Thomas Schuhmann, Alexander Conradi, Christian Deeg, Konrad Brandl:

Determination of Stator End Winding Inductance of Large Induction Machines: Comparison Between Analytics, Numerics, and Measurements, Electric Power Components and Systems

HTWD Hochschule für Technik und Wirtschaft Dresden
University of Applied Sciences

Qucosa
Quality Content of Saxony

Determination of Stator End Winding Inductance of Large Induction Machines: Comparison Between Analytics, Numerics, and Measurements

THOMAS SCHUHMANN,[1] ALEXANDER CONRADI,[2]
CHRISTIAN DEEG,[1] and KONRAD BRANDL[1]

[1]Siemens AG, Industry Sector, Drives Technology Division,
Nuremberg, Germany
[2]Department of Electrical Drives and Mechatronics, Dortmund University of
Technology, Dortmund, Germany

Abstract *Knowledge of the end winding inductance of electrical machines is decisive for calculating their operating performance. In this article, two different approaches to analytically calculate the stator end winding inductance of large induction machines are discussed. The first method is based on the exact replication of the 3D conductor geometry using serially connected straight filaments, where the inductances are calculated by solving Neumann's integral. In the second method, the end winding flux is resolved into components excited by the axial and circumferential end winding magnetomotive force, resulting in a far simpler geometrical model. In both cases, end face effects are taken into account by adopting the method of images. The analytical approaches are compared to the known analytical calculation method proposed by Alger [1]. In addition, the stator end winding inductance is computed by means of 3D finite-element analysis. Using experimental validation, it is shown that both the analytical and numerical results reasonably correlate with removed rotor inductance measurements taken for several induction machines with different rated powers and frame sizes, if the permeability of the laminated core is taken into consideration.*

Keywords electrical machines, end winding inductance, analytical model

1. Introduction

Knowledge of the leakage inductance of electrical machines is essential for determining their operational performance in particular starting torque, starting current, power factor, and (relative) short-circuit voltage [2, 3]. One major component of the leakage inductance is the inductance of the end winding (*i.e.*, the part of the winding outside the core region connecting the single coil sides located under different poles). When cross-sectional 2D finite-element computations of electrical machines are to be performed, the end region parameters also have to be known in order to obtain meaningful results [4]. Especially for two-pole machines with their large coil span and winding overhang, the end winding

leakage inductance represents a considerable percentage of the overall leakage inductance, which can exceed 50%.

Contrary to "classic" magnetic leakage fields in electrical machines (*e.g.*, slot, tooth tip, and zigzag leakage), the end winding field is characterized by a complicated 3D pattern [1]. Typically, the end winding inductance (which is one element of the single-phase equivalent circuit of an AC machine) is calculated by means of simple approximation equations, using constant magnetic leakage permeances [5]. These leakage permeances are based on experimental data or on the long-time experience of the manufacturers. However, these rough approaches do not allow the actual 3D end winding geometry to be taken into consideration. Especially when changes in machine design or frame size are required, the traditional leakage permeances lose their validity.

In recent years, numerous approaches for a more detailed calculation of the end winding inductances of electrical machines have been published, taking into account the exact geometry of the winding overhang. Several authors have proven the applicability of numerical 3D field computations for this purpose. In [6], the end winding leakage inductance of a high-speed generator is calculated using a 3D finite-difference method. The use of 3D finite-element analysis (FEA) to calculate the stator end winding inductance of AC machines was discussed in [7–9] and elsewhere. Further, the frequency dependency of the end winding leakage inductance of an induction machine stator was discussed in [10]. Other works were dedicated to the numerical computation of the end winding inductance of permanent-magnet linear synchronous motors [11]. The calculation of the end winding inductances of large synchronous machines based on 3D FEA was discussed in [12, 13]. A comparison of the results of an analytical and a numerical calculation of the end winding inductance of a turbo generator was presented in [14].

Nevertheless, the use of 3D finite-element tools implicates several disadvantages. First, modeling of the 3D coil geometry is very time consuming. Furthermore, to reach converging solutions, a very large number of elements may be necessary, especially if particular boundary conditions are to be taken into account, such as the relative permeability of the end plates, which considerably increases the computation time. Finally, elaborate post-processing is needed to obtain the correct leakage inductance value per phase from the huge amount of data generated. This is why numerical calculation of the end winding inductances presently does not appear to be suitable for efficiently designing industrial electrical machines. Analytical approaches that take into account the geometry of the end winding coils are more suitable for this purpose and can be solved in a few seconds or less. Such methods are presented together with others in [1, 14–18].

Two different analytical approaches to calculate induction machine stator end winding inductances are presented in detail in this article. The first is based on the approaches introduced in [16, 17], where each stator conductor is replaced by serially connected filaments and inductances are obtained by solving Neumann's integral. The second applies a simpler geometrical model by breaking down the end winding flux into different components produced by the axial and circumferential end winding magnetomotive force (mmf), as already suggested in [1]. The results of both analytical models are compared to the analytical calculation method described by Alger [1] and numerical 3D FEA computations as well as removed rotor measurements on a broad range of large induction machines.

2. End Winding Geometry and Assumptions

The electrical machines discussed in this article are high-voltage three-phase squirrel-cage induction machines in the power range of 220 to 1330 kW, with frame sizes in the
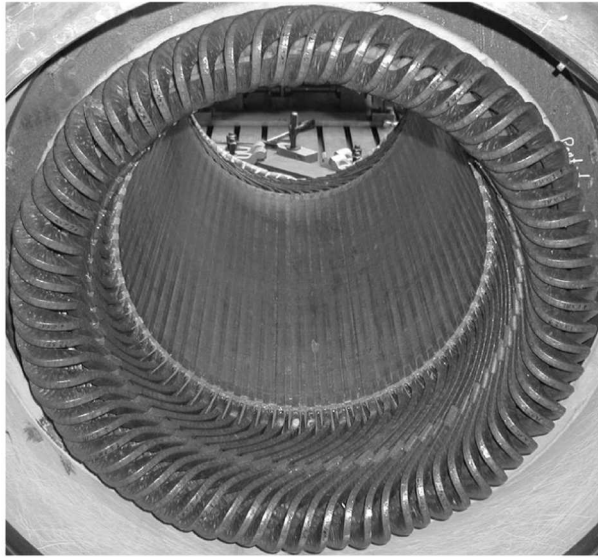
Figure 1. View of back end of high-voltage induction motor with end winding region (rotor removed).

range of 315 to 560 mm and pole numbers in the range of 2 to 10. The short-pitched, two-layer stator winding is manufactured as a form-wound diamond-shaped winding, as can be seen in Figure 1. The geometrical model of the end winding coils used for the calculations is based on a parametric involute model discussed in detail in [16].

The problem of defining a mutual inductance of the (open-ended) end winding coils was already mentioned in [10, 16]. Nevertheless, in this article, the term "inductance" is used, denoting the flux linkage of one current-carrying end region conductor with another end region conductor, including flux elements partially passing into the core and excluding fringe elements of the air gap flux. For the analytical models, the following assumptions apply.

(a) The influence of the end plate and the laminated core is taken into account using the method of images. The iron surface delimits an infinite half-space. The relative permeability of the iron core is regarded as constant and isotropic; the end winding conductors are completely located in air.
(b) Other design elements (*e.g.*, shaft, bearing shield, housing) as well as the influence of slots and air gap are neglected.
(c) The stator winding is fed from a symmetrical three-phase system.
(d) Only the fundamental mmf component is considered.

3. Analytical Model I: Neumann Integrals

Considering the exact geometry of the coils in the end winding region, the end winding inductances for single coils can be calculated by applying Neumann's integral and the method of images [14–17]. To obtain the end winding inductance of one phase for use in the single-phase equivalent circuit model, the inductances at the coil level are further

processed by considering the precise interconnection of the single coils as described in Section 3.3.

3.1.   Calculation of Inductances at Coil Level in Air

Mutual inductances between two loops of infinitely thin conductors v and k of any 3D shape in air can be calculated by solving Neumann's integral:

$$M_{vk} = \frac{\mu_0}{4\pi} \cdot \int_{l_v} \int_{l_k} \frac{d\vec{l}_v \cdot d\vec{l}_k}{r_{vk}} = \frac{\mu_0}{4\pi} \cdot \int_{l_v} \int_{l_k} \Gamma. \tag{1}$$

Here, l describes the path along a loop, and r_{vk} represents the distance between the two differentials $d\vec{l}_v$ and $d\vec{l}_k$ on loop v and k currently being considered with the integration. By considering the winding numbers w_v and w_k, Eq. (1) can be equally applied to coils with more than one turn along the same path.

In order to be able to analytically carry out the integration, each coil is further modeled as a series of n straight filaments, which is also permissible for conductors with a finite cross-section if the length of each filament is large compared to the cross-section edges [19]. In addition to this condition, the number of straight filaments can be chosen arbitrarily so that the desired geometrical accuracy is reached. The mutual inductance between two coils v and k is then calculated by applying Eq. (1) on each combination of the single filament segments of coil v with those of coil k:

$$M_{vk} = w_v w_k \frac{\mu_0}{4\pi} \cdot \sum_{m_v=1}^{n_v} \sum_{m_k=1}^{n_k} \int_{l_{m_v}} \int_{l_{m_k}} \frac{d\vec{l}_{m_v} \cdot d\vec{l}_{m_k}}{r_{m_{vk}}}. \tag{2}$$

To calculate the self-inductances (*i.e.*, $v = k$) of the coils, the application of Eq. (2) is restricted to the mutual inductances between the single straight filament sections of the coil. According to [17], the self-inductance of a section can be obtained by calculating the mutual inductance (*cf.*, Eq. (2)) of the regarded filament section with a parallel filament of the same length at the geometrical mean distance (GMD) for each pair of two points within the cross-section A of the conductor, defined by

$$\ln(GMD) = \frac{1}{A^2} \int_A \int_A \ln(s) dA dA, \tag{3}$$

where s denotes the distance between the two points.

3.2.   Calculation of Machine End Winding Inductances at Coil Level

According to the definition in Section 2, only the contributions of the end parts of the coils to the mutual inductances are considered, so that when applying Eq. (2), l_v and l_k only represent the paths along the parts of the coil in the end winding section located in air.

As Neumann's integral can only be applied to spaces of homogenous permeability, the influence of the iron core (which is bounding the air-filled end winding region) on the magnetic field is modeled by using the method of images as described in [16], which requires the assumptions (a) and (b) made in Section 2.

Any coil having a finite length in air and crossing the bonding surface between the half-spaces perpendicularly can be constructed by superposition of infinite circuits, as depicted in the principle model in Figure 2, configuration (A).
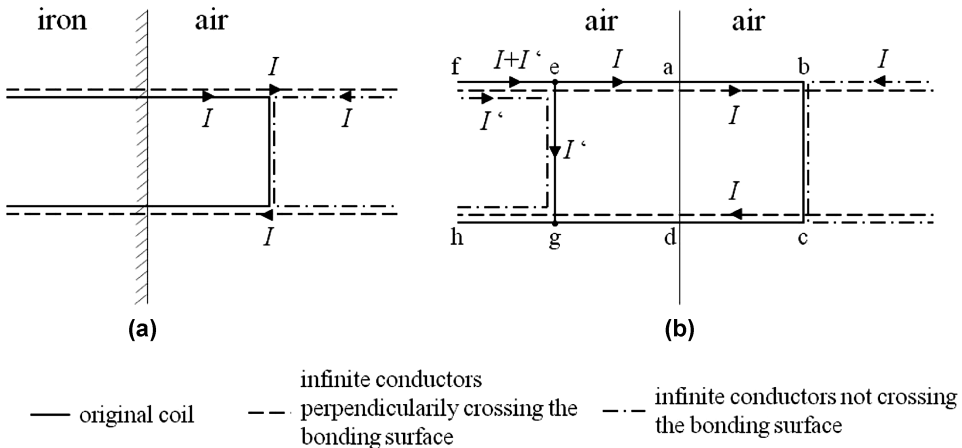
According to [16], by creating a mirror image of the infinite conductors not crossing the bonding surface, configuration (A), containing two half-spaces comprising iron and air respectively, can be equally modeled with two half-spaces both comprising air in configuration (B). The inductances of the transformed configuration (B) can subsequently be calculated using Neumann's integral.

The permeability of the iron in configuration (A) can be considered in configuration (B) by the current I' flowing in the mirrored conductor, which can be calculated with the image factor k_m as:

$$I' = k_m I = \frac{\mu_r - 1}{\mu_r + 1} I, \tag{4}$$

where μ_r is the relative permeability of the iron, and I is the current of the original conductor. For the configuration in Figure 2, the self-inductance of the segment of the original coil in air with winding number w, defined as the end winding inductance in Section 2, can then be calculated as

$$
M = w^2 \frac{\mu_0}{4\pi I} \left(I \cdot \left(\int_{ab}\int_{bd} \Gamma + \int_{bc}\int_{ab} \Gamma + \int_{bc}\int_{cd} \Gamma + \int_{cd}\int_{ac} \Gamma \right. \right.
$$

$$
+ \int_{ab}\int_{ab} \frac{d\vec{l}_1 \cdot d\vec{l}_2}{GMD} + \int_{bc}\int_{bc} \frac{d\vec{l}_1 \cdot d\vec{l}_2}{GMD} + \int_{cd}\int_{cd} \frac{d\vec{l}_1 \cdot d\vec{l}_2}{GMD} \right)
$$

$$
+ \int_{ad} \left(I \cdot \left(\int_{ea} \Gamma + \int_{dg} \Gamma \right) + I' \cdot \int_{eq} \Gamma + (I + I') \right.
$$

$$
\left. \left. \cdot \left(\int_{fe} \Gamma + \int_{gh} \Gamma \right) \right) \right). \tag{5}
$$

Figure 2. Principle model of open-ended coil with finite length in air and perpendicular crossing of the bonding surface between air and iron half-space.

To calculate the stator end winding inductance at the phase level for use in the standard single-phase equivalent circuit model, the inductances at the coil level, which can be calculated as in the above example, first have to be merged to create higher level inductance matrices. This will be described in the following section.

3.3. Calculation of Machine End Winding Inductances at Phase Level

Calculation of the one-sided self- and mutual inductances of all N stator coils in the end winding section of the machine, as described in Section 3.2, yields the symmetrical $N \times N$ matrix $\mathbf{M}_{coil}$. To obtain the stator end winding inductance at the phase level, the inductances of $\mathbf{M}_{coil}$ first have to be merged at the coil group level, and finally to phase level inductance matrices $\mathbf{M}_{cg}$ and $\mathbf{M}_{phase}$, as described in [17]. For machines with three-phase windings in the abc-scheme and q slots per pole and phase, the required connection matrices are formed as

$$
\mathbf{C} = \left(\overbrace{\begin{array}{cccccccccccc}
1 & 1 & \cdots & 1 & 0 & 0 & \cdots & 0 & \cdots & 0 & 0 & \cdots & 0 \\
0 & 0 & \cdots & 0 & 1 & 1 & \cdots & 1 & \cdots & 0 & 0 & \cdots & 0 \\
\vdots & \vdots & \vdots & \vdots & \vdots & \vdots & \vdots & \vdots & \ddots & \vdots & \vdots & \vdots & \vdots \\
0 & 0 & 0 & 0 & 0 & 0 & 0 & 0 & \cdots & 1 & 1 & \cdots & 1
\end{array}}^{q} \right) \left.\vphantom{\begin{array}{c}1\\0\\\vdots\\0\end{array}}\right\} \tfrac{N}{q} \tag{6}
$$

and

$$
\mathbf{D} = \overbrace{\begin{pmatrix}
1 & 0 & 0 & -1 & 0 & 0 & \cdots & \cdots \\
0 & 0 & 1 & 0 & 0 & -1 & \cdots & \cdots \\
0 & -1 & 0 & 0 & 1 & 0 & \cdots & \cdots
\end{pmatrix}}^{\frac{N}{q}}. \tag{7}
$$

Two-sided linear multiplication, taking into consideration the number of parallel coil groups per phase g_{par}, then yields $\mathbf{M}_{cg}$ and $\mathbf{M}_{phase}$:

$$
\mathbf{M}_{cg} = \mathbf{C} \cdot \mathbf{M}_{coil} \cdot \mathbf{C}^{\mathbf{T}}, \qquad \mathbf{M}_{phase} = \frac{1}{g_{par}^2} \mathbf{D} \cdot \mathbf{M}_{cg} \cdot \mathbf{D}^{\mathbf{T}} = \begin{pmatrix} M_{aa} & M_{ab} & M_{ac} \\ M_{ba} & M_{bb} & M_{bc} \\ M_{ca} & M_{cb} & M_{cc} \end{pmatrix}. \tag{8}
$$

As $\mathbf{M}_{phase}$ is symmetrical due to the uniformly shaped coils, the single-phase inductance for both end winding sections L_e is equal for all phases. For example, the induced voltage $v_{a,e}$ in the end winding of phase a in both end winding sections of the machine can be calculated with the elements from $\mathbf{M}_{phase}$ and is given by

$$
v_{a,e} = 2 \cdot \frac{d}{dt}(M_{aa} \cdot i_a + M_{ab} \cdot i_b + M_{ac} \cdot i_c) = 2 \cdot (M_{aa} - M_{ab})\frac{d}{dt}i_a, \tag{9}
$$

thus yielding

$$L_e = 2 \cdot (M_{aa} - M_{ab}). \tag{10}$$

4. Analytical Model II: Resolution of End Winding Flux into Components

The mmf in the end winding region exhibits an axial, a circumferential, and a (smaller) radial component (see Figure 1). The simplified analytical calculation presented in this section makes a basic assumption that the end winding flux can be resolved into components due to the principle of superposition [1]. The following elements are taken into account:

- a component excited by circumferential mmf, assigned to "circumferential" end winding inductance L_{ec};
- a component excited by axial mmf, assigned to "axial" end winding inductance L_{ea};
- a component excited by mmf in the "nose" part (Figure 3), assigned to the nose end winding inductance L_{en}.

4.1. Calculation of the Circumferential Component

Circumferential mmf components are encountered in the skewed part of the stator winding overhang, characterized by the axial width b (see Figure 3).

The method of images is applied to calculate the inductance L_{ec} assigned to the circumferential components of the stator conductors. A substitute circular conductor loop with the mean diameter D_m, located in the geometrical center of the skewed part, is introduced for this purpose (see Figure 4). The influence of the stator core is taken into account by assuming its surface as an infinite half-plane, thus replacing it by image conductors [20–22], as already stated in Section 3.2. The image current I'_{ec} depends on the true current I_{ec} according to

$$I'_{ec} = k_m I_{ec} = \frac{\mu_r - 1}{\mu_r + 1} I_{ec}, \tag{11}$$

with the image factor k_m allowing an arbitrary relative permeability μ_r of the core region to be taken into account [16]. Magnetically ideal iron with $\mu_r \to \infty$ would lead to an image factor of 1. Yet for higher frequencies, the circumferential component of the end zone current may induce eddy currents in the core that produce additional losses and reduce the leakage reactance; this case can be taken into account by reducing the core permeability, which results in a smaller image factor. The flux connected with the substitute conductor can be calculated by evaluating the magnetic vector potential on a circular path of integration located in four equally distributed computation points P_1 to P_4 (Figure 4). The distance r_P between each computation point and the center of the substitute conductor depicts the mean geometrical distance of the conductor to itself [23]. It is calculated by

$$r_P = \frac{e^{(\frac{\pi}{3} - \frac{25}{12})}}{\sqrt[3]{4}} (b + h), \tag{12}$$
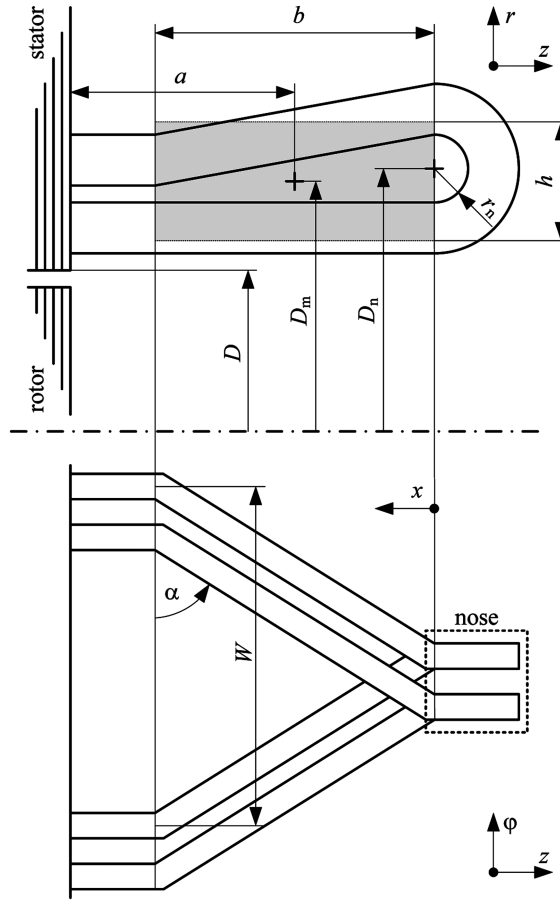
**Figure 3.** Longitudinal section and top view of stator end winding region.

with b the width and h the mean height of the skewed part of the stator end winding coil (Figure 3). For each computation point, the vector potential of a circular conductor loop has a circumferential component

$$A_c = \frac{\mu_0 I^*}{2\pi r} \sqrt{(z^*)^2 + (r_0^* + r^*)^2} \cdot \left[\left(1 - \frac{k^2}{2}\right) \cdot K(k) - E(k) \right] \qquad I^* \in [I_{ec}, I'_{ec}],$$

(13)

with

$$k = \sqrt{\frac{4 r_0^* r^*}{(z^*)^2 + (r_0^* + r^*)^2}}.$$

(14)

The expressions $K(k)$ and $E(k)$ in Eq. (13) denote complete elliptical integrals of the first and second kinds. For each computation point P_1 to P_4, the radii of the current-carrying (source) conductor r_0^* and of the computation point r^* as well as the axial distance z^* between the source conductor and the computation point have to be chosen, as shown
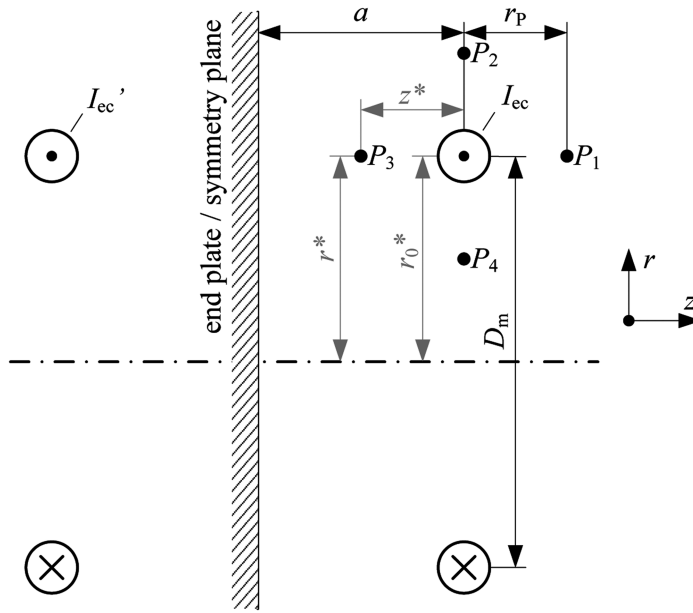
Figure 4. Application of method of images for calculating circumferential part of stator end winding inductance (dimensions r^*, r_0^*, and z^* are shown exemplarily for calculating the vector potential of I_{ec} in computation point P_3).

exemplarily in Figure 4. The vector potential in one computation point is to be calculated by adding the results of Eq. (13) for the true current I_{ec} and for the image current I'_{ec}. The magnetic flux is then calculated by

$$\Phi_{ec} = \oint A_c \, ds = \int_0^{2\pi} A_c r \, d\varphi = 2\pi r \cdot A_c; \tag{15}$$

the mean value is then generated over the four computation points. The magnetic leakage permeance of the circumferential stator conductor is then obtained by

$$\lambda_{ec} = \frac{\Phi_{ec}}{\mu_0 \pi D_m I_{ec}}, \tag{16}$$

which in turn yields the circumferential stator end winding inductance

$$L_{ec} = 2\mu_0 l_e \cos^2 \alpha \frac{w_1^2}{p} \cdot \left(\lambda_{ec} + \frac{1}{8\pi} \right), \tag{17}$$

with l_e as the stator end winding conductor length in the skewed part, α the skewing angle of the diamond-shaped winding (Figure 3), w_1 the number of turns per phase, and p the number of pole pairs. The term $1/(8\pi)$ is included to take into account the inner self-inductance of the conductors [16].

4.2. Calculation of the Axial Component

Axial components of the mmf can be observed in the straight overhang and in the skewed part of the stator end winding (Figure 3). The flux excited by these currents is assumed to

flow in radial planes [1], which means that the influence of the iron core can be neglected here. The calculation of the axial stator end winding inductance is based on a modified approach for calculating the removed rotor inductance [24] given by

$$L_{ea,unskewed} = \frac{3}{\pi}\mu_0(w_1\xi_1)^2\frac{1}{p} \cdot \left(2a + \frac{D}{8p}\right).$$ (18)

with ξ_1 the winding factor of the fundamental wave, D the stator inner diameter, and a the axial distance between the end plate and geometrical center of the skewed part of the end winding. The term $(D/8p)$ is included to take into account the axial spread of the field. Due to skewing of the coils, the coil span reduces from W at $x = b$ to 0 at $x = 0$ (Figure 3). Thus, the winding factor becomes a function of x and can be expressed as

$$\xi_1(x) = \frac{3}{\pi}\sin\left(\frac{W}{\tau}\frac{\pi}{2}\frac{x}{b}\right),$$ (19)

where τ denotes the stator pole pitch. The contribution of each differential plane dx on the axial stator inductance can be taken from Eqs. (18) and (19) as

$$\Delta L_{ea} = \frac{3}{\pi}\mu_0\left(w_1 \cdot \frac{3}{\pi}\sin\left(\frac{W}{\tau}\frac{\pi}{2}\frac{x}{b}\right) \cdot \sin\alpha\right)^2\frac{1}{p} \cdot (2dx).$$ (20)

The term $\sin\alpha$ considers that only the axial component of the end winding current is taking effect. Integrating Eq. (20) from $x = 0$ to b, and adding the contributions of the straight overhang $(2a-b)$ and the axial field spread $(D/8p)$, the axial stator end winding inductance is given by

$$L_{ea} = \frac{3}{\pi}\mu_0(w_1\xi_1)^2\frac{1}{p}\left[(2a - b) + b\left(1 - \frac{\sin\left(\frac{W}{\tau}\pi\right)}{\frac{W}{\tau}\pi}\right)\left(\frac{3\sin\alpha}{\pi\xi_1}\right)^2 + \frac{D}{8p}\right].$$ (21)

4.3.   Calculation of the Nose Component

In addition to inductance components assigned to tangential and axial conductors, the diamond-shaped stator winding excites flux components attached to the nose and the outer parts of the skewed coil sides (Figure 3). The inductance assigned to this flux component can be roughly estimated by

$$L_{en} \approx \frac{12}{\pi}\mu_0(w_1\xi_1)^2\frac{r_n}{D_n}\left(r_n\pi + \frac{4}{3}b\sin^2\alpha\right),$$ (22)

with r_n the radius of the winding mandrel of the nose and D_n the diameter of the geometrical center of the nose (Figure 3).

4.4.   Combination of Inductance Components

Applying the principle of superposition, the inductances calculated for the different flux components have to be added to obtain the subtotal stator end winding inductance per phase:

$$L_e = L_{ec} + L_{ea} + L_{en}.$$ (23)

5. 3D Finite-element Computation

To validate the correctness of the analytical calculation methods, the stator end winding inductance was calculated using 3D FEA with the tool ANSYS Maxwell 3D (ANSYS, Inc., Canonsburg, Pennsylvania, USA). The following simplifications apply.

- The stator winding has been modeled by current-driven, stranded coils located in air; each coil consists of one turn.
- The cross-section of one coil is approximated as a square; the nose region is simplified as a straight junction.
- The model has been cut at the end plate surface.
- Two boundary conditions apply at the end plate surface—either tangential flux (Neumann boundary condition [b.c.]) or normal flux (even symmetry)—according to a relative permeability of the iron core of $\mu_r = 0$ (tangential flux) or $\mu_r \to \infty$ (normal flux).

For example, the geometrical end winding model of machine II (*cf.*, Table 1 in Section 7) is shown in Figure 5.

Based on the above-mentioned simplifications, the matrix of the self- and mutual inductances of the single end winding turns is calculated as follows. First the magnetostatic field problem is solved for all coils fed from a symmetrical three-phase current system. The single coils are then fed sequentially with a current of 1 A, and a separate field calculation is carried out in each case, yielding the distribution of the magnetic flux density and the magnetic field strength for the problem region. The self- and mutual inductances of two coils v and k are then calculated by evaluating the energy integral over the problem region Ω ($I_v = I_k = 1$ A):

$$L_{vk} = \int \int \int \vec{B}_v \vec{H}_k d\Omega, \tag{24}$$

yielding the stator end winding inductance matrix $\mathbf{M}_{turn}$ at the turn level. To obtain the end winding inductance L_e per phase, $\mathbf{M}_{turn}$ first has to be multiplied by the square
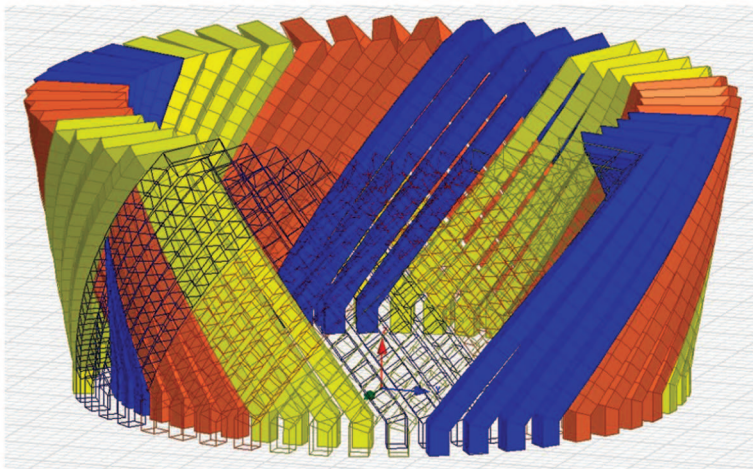
Figure 5. 3D FEA geometrical model of stator end winding (machine II, $2p = 4$ poles, coils of 1 pole transparently shown). (color figure available online)

of the number of turns w per coil to obtain the inductance matrix at the coil level ($\mathbf{M}_{coil} = w^2 \mathbf{M}_{turn}$). $\mathbf{M}_{coil}$ then has to be reduced to the coil group level and finally to the phase level, as described in Section 3.3.

6. Removed Rotor Measurements

6.1. Measurement of Stator Phase Inductance

During the removed rotor test, rotor and bearing shields are disassembled, and the stator winding is fed with the rated symmetrical three-phase current [24, 25]. The stator inductance per phase is calculated by

$$L_1 = \frac{1}{2\pi f_1} \cdot \sqrt{\left(\frac{V_S}{I_S}\right)^2 - \left(\frac{P}{3I_S^2}\right)^2}, \tag{25}$$

with V_S and I_S the measured stator voltage and current per phase, P the overall measured active power, and f_1 the supply frequency.

6.2. Calculation of Stator End Winding Inductance

For the removed rotor test, the overall stator inductance L_1 consists of the components

- slot and tooth tip leakage inductance L_s;
- end winding inductance L_e; and
- inductance L_b assigned to the main bore field, which occurs within the range of the disassembled rotor.

To separate the end winding inductance L_e from the measured stator inductance L_1, the additional components L_s and L_b have been calculated using 2D magnetostatic FEA with the tool FEMAG DC (Institute for Electrical Machines at Swiss Federal Institute of Technology [ETH], Zurich) (Prof. K. Reichert). In Figure 6, the magnetic field lines representing the slot, tooth tip, and bore field inside the core region are illustrated for machine II at the rated stator current.

As mentioned in [24, 25], to calculate the bore field inductance L_b, the axial spread of the field at the machine ends has to be taken into account. Therefore, the value $L_{b,FEA}$ calculated by FEMAG DC is increased by an additional component, yielding the expression

$$L_b = L_{b,FEA} + \underbrace{\frac{6}{\pi}\mu_0(w_1\xi_1)^2\frac{1}{p}\cdot\frac{\tau}{6}}_{\text{axial field spread}}. \tag{26}$$

With the measured inductance per phase given by Eq. (25) and the numerically calculated values for the slot, tooth tip, and bore field inductance, taking into account the axial field spread of the bore field based on Eq. (26), the end winding inductance per phase is finally determined by

$$L_e = L_1 - L_s - L_b. \tag{27}$$
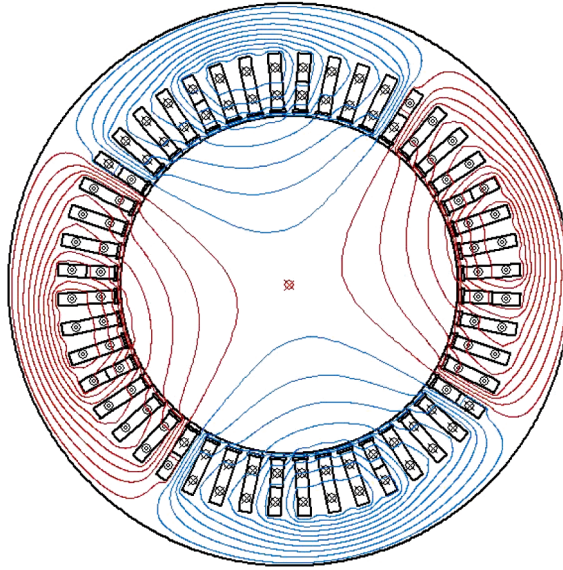
Figure 6. Magnetic field distribution inside core of machine II at rated stator current, calculated by 2D FEA. (color figure available online)

7. Comparison of Results

Finally, a comparison is drawn up between the different calculation and measurement results. The basic parameters of the induction machines being investigated are listed in Table 1.

It has been mentioned that analytical models I and II are capable of taking into account the stator core permeability. Initially, the results for the boundary condition $\mu_r = 0$ (tangential flux, field lines do not enter the stator core) will be discussed. It is obvious that this boundary condition cannot be applied in practice using removed rotor measurements; as a consequence, no measurement results are given in this case. Instead, the results of the known analytical calculation method described by Alger [1] are given, a method that is valid only for the previously mentioned boundary condition $\mu_r = 0$. The end winding inductances per phase for machines I to VII are displayed in Figure 7.

Table 1
Investigated machines

| No.	Rated power, P_r (kW)	Number of poles, $2p$	Shaft height (mm)
I	650	2	400
II	365	4	315
III	1330	4	560
IV	220	6	315
V	425	6	355
VI	465	8	400
VII	416	10	450

As can be seen, the results of the analytical models correlate very well with the 3D FEA calculations. In particular, the Neumann method (analytical model I) correlates very well with the numerical field calculation for this boundary condition. With increasing pole number, the end winding inductance decreases due to the smaller pole pitch and thereby a smaller end winding conductor length.

The end winding inductances for the boundary condition $\mu_r \to \infty$ (normal flux, field lines enter the stator core perpendicularly) are shown in Figure 8. In addition to the results of the analytical models (I and II) and the numerical computation, the measured values, calculated as delineated in Section 6.2, are shown. As expected, the inductances are generally greater than the values for the tangential flux b.c. This is due to the higher magnetic conductivity in the stator core range. It is notable in this case that analytical models I and II show a higher discrepancy than for $\mu_r = 0$, especially for the two-pole machine I. On average, analytical model II has the best correlation to the measured values. Nevertheless, the deviation between calculation and measurement is up to 61% for the higher pole machines. In most cases, the measured inductances are bigger than those analytically calculated. This fact is surprising because most of the effects not considered in the calculation model (*e.g.*, eddy currents in surrounding parts, skin effect) would lead to a reduction of the end winding inductance. One possible explanation is the uncertainty due to the indirect measurement method (Section 6.2), because, especially for higher pole machines, the percentage of the end winding inductance in the overall inductance is low, and inaccuracies in the inductances L_1, L_s, and L_b become more influential (*cf.*, Eq. (27)). Other possible reasons for this behavior have still to be identified.

As described in Sections 3.3 and 5, when applying analytical model I (Neumann integrals) and the 3D FEA, the end winding inductances are calculated in successive steps (turn level $\to$ coil level $\to$ coil group level $\to$ phase level). Therefore, these results can be investigated in more detail by comparing inductances at the single coil
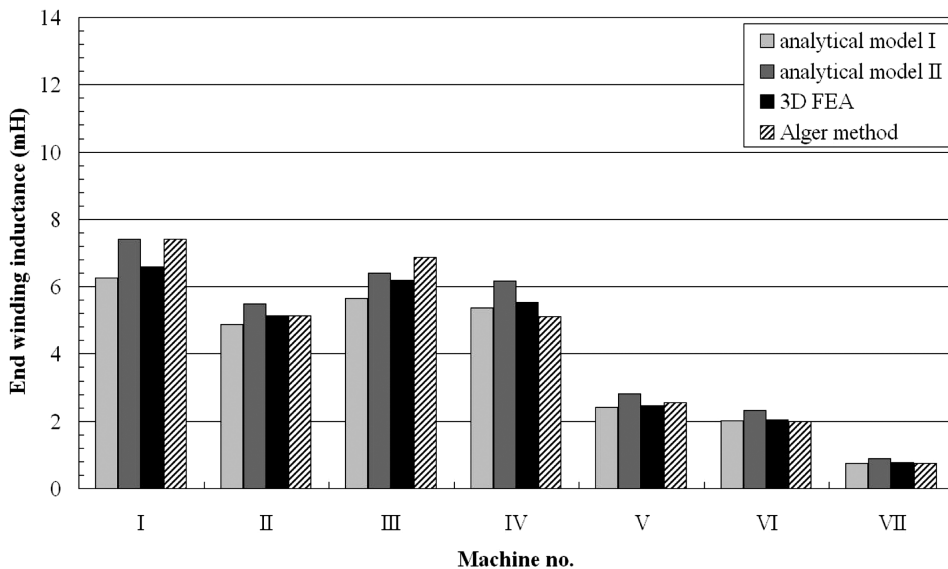
Figure 7. Comparison of analytically and numerically calculated single-phase end winding inductances (boundary condition: tangential flux, $\mu_r = 0$).
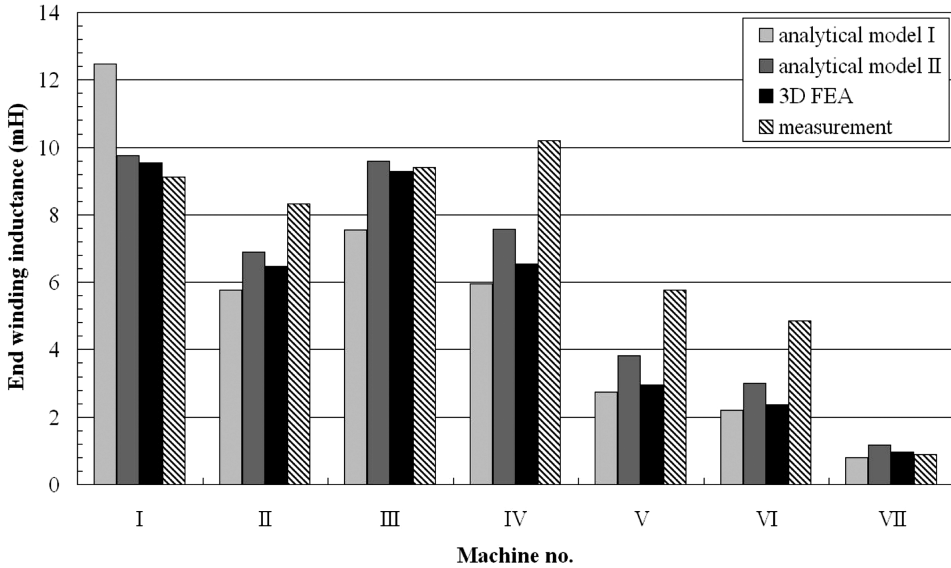
Figure 8. Comparison of analytically and numerically calculated as well as measured single-phase end winding inductances (boundary condition: normal flux, $\mu_r \to \infty$).

and coil group levels. Figures 9 and 10 exemplarily show the calculated inductances for machine I (48 coils in 6 coil groups), which gives an adequate basis for discussion, as similar characteristics can be observed for the other machines being investigated. In Figure 9, inductances are depicted for one single coil with itself (index 1) and with all successive coils along the circumference (ascending index). The same scheme applies for the diagram showing the coil group inductances.

As can be expected, except for the self-inductances denoted with index 1, the diagrams show perfect symmetry for the position of the flux-linking coils along the circumference. Furthermore, assuming that the flux enters the iron core (i.e. $\mu_r \to \infty$), it is plausible that absolute values of the inductances are predominantly higher than when assuming tangential flux at the boundary.

Similar to the results for the phase inductances, the results calculated with the boundary condition of tangential flux ($\mu_r = 0$) show excellent correlation between the different calculation methods at both the single coil and coil group levels. For normal flux ($\mu_r \to \infty$), a higher deviation has been observed in the single-phase inductance results (Figure 8) between the Neumann method and the 3D FEA as well as analytical model II (resolution of flux components), respectively. To a considerable extent, this obviously comes from different mutual inductances between the coils with negative flux linkage to each other (zone of negative flux linkage), for which the Neumann method calculates mutual inductances with substantially higher absolute values than 3D FEA.

8. Conclusion

The objective of this article is to provide a comparison between different analytical methods for calculating the stator end winding inductance of high-voltage induction machines. Two analytical models have been presented in detail—the first model (solution
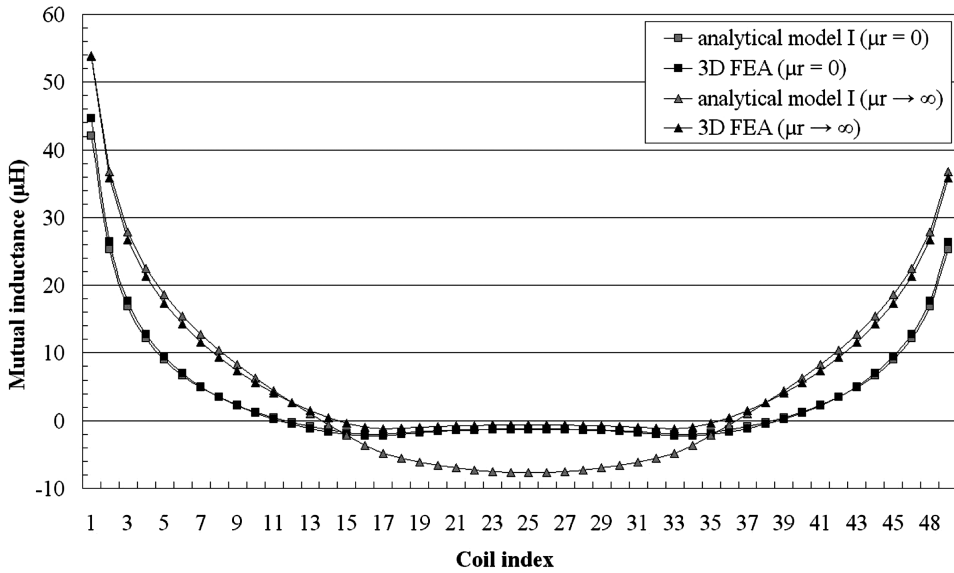
Figure 9. Comparison of analytically and numerically calculated inductances at coil level for machine I.
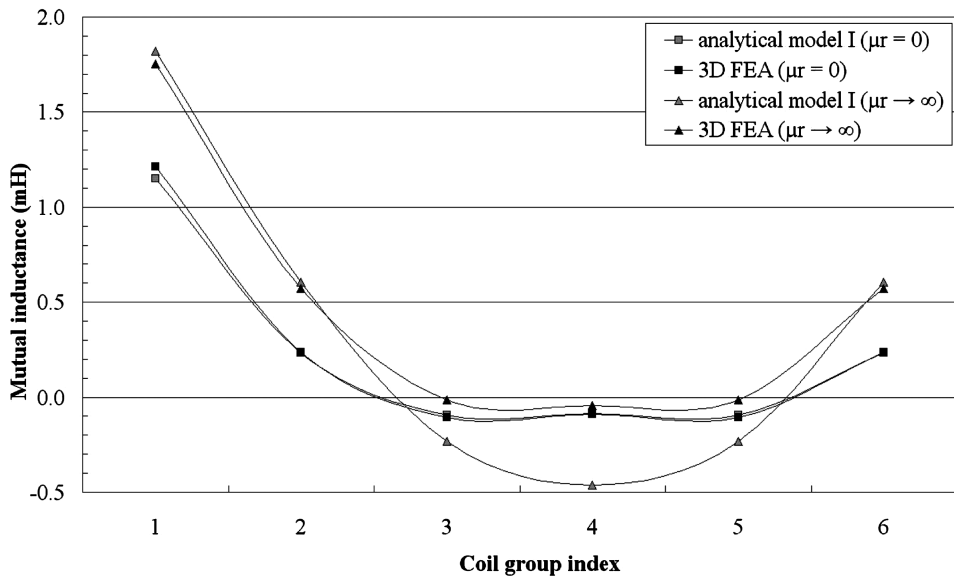

Figure 10. Comparison of analytically and numerically calculated inductances at coil group level for machine I.

of Neumann integrals), which is based on the work in [14–17], and the second model (resolution of end winding flux into components), which represents original work. The results of both analytical models have been compared to the known analytical method of Alger [1], to numerical 3D FEA calculations, and, in particular, to measurements made on a broad range of different induction machines.

The results show that for the boundary condition of tangential flux ($\mu_r = 0$) at the axial machine end plates, the different analytical models (Neumann, flux resolution, Alger) correlate very well with each other and with numerical field calculations. The analysis at the single coil level particularly confirms the excellent correlation between the analytical Neumann method (analytical model I) and the 3D FEA.

Nevertheless, the removed rotor measurement results indicate that to calculate the end winding inductance of rotating electrical machines, the end plate boundary condition has to be set to normal flux ($\mu_r \to \infty$) for low frequencies, as the grid frequency in the present investigation. This means that the magnetic field amplification due to the laminated iron core must be considered. For higher frequencies, smaller permeability values may be appropriate for taking into account the reduction of the leakage reactance due to eddy currents in the core induced by the circumferential end zone current component. The boundary condition $\mu_r \to \infty$ cannot be represented using the Alger method, which thus results in inductances that are too low. However, analytical models I and II have the necessary capacity of taking into account arbitrary core permeabilities.

The best correlation between theoretical results and experimental data is obtained with analytical model II (resolution of end winding flux into components). In addition, this model uses a more simple geometric approach and can be implemented more easily than model I (solution of Neumann integrals). On the other hand, model I provides the opportunity of performing investigations at the single coil level, which may be helpful for analyzing unsymmetrical windings. Compared to numerical 3D FEA, both analytical models investigated in this study allow the stator end winding inductance to be reasonably estimated within a small fraction of the time required for the numerical field solution. This makes them suitable for industrial machine design processes.

Ongoing work will focus on adapting the analytical models for calculating the end winding inductance of the rotor cage as well as the end region coupling inductance between stator and rotor. In addition, a geometrical model for random-wound low-voltage windings will be implemented. Beyond that, the influence of higher stator frequencies on the reduction of the end winding inductance due to eddy currents in the core as well as skin effect has to be studied, which may be of interest for high-speed inverter-fed machines.

References

1. Alger, P. L., *Induction Machines—Their Behavior and Uses*, 2nd ed., New York: Gordon and Breach, pp. 233–243, 1970.
2. Nicolas, R., Marcel, I., and Demba, D., "Modeling and experimental study of 3-phase short-circuits of a double-cage induction machine," *Elect. Mach. Power Syst.*, Vol. 27, pp. 343–362, 1999.
3. Gross, C.A., and Nelms, R. M., "A comparison of two analytical methods of determining the starting transients of a single-phase induction machine," *Elect. Mach. Power Syst.*, Vol. 19, pp. 705–712, 1991.
4. De Weerdt, R., Tuinman, E., Hameyer, K., and Belmans, R., "Finite element analysis of steady state behavior of squirrel cage induction motors compared with measurements," *IEEE Trans. Magnet.*, Vol. 33, No. 2, pp. 2093–2096, March 1997.

5. Oberretl, K., "Influence of skin effect on mutual inductance of double-cage induction motors," *Elect. Eng.*, Vol. 87, pp. 103–111, 2005.

6. Sarma, M. S., Wilson, J. C., Lawrenson, P. J., and Jokl, A. L., "End-winding leakage of high-speed alternators by three-dimensional field determination," *IEEE Trans. Power App. Syst.*, Vol. PAS-90, No. 2, pp. 465–477, March/April 1971.

7. Brahimi, A. T., Foggia, A., and Meunier, G., "End winding reactance computation using a 3D finite element program," *IEEE Trans. Magnet.*, Vol. 29, No. 2, pp. 1411–1414, March 1993.

8. Chiver, O., Micu, E., and Barz, C., "Stator winding leakage inductances determination using finite elements method," *Proceedings of 11th International Conference on Optimization of Electrical and Electronic Equipment (OPTIM)*, Brasov, Romania, 22–24 May 2008.

9. Cox, T., Eastham, F., and Proverbs, J., "End turn leakage reactance of concentrated modular winding stators," *IEEE Trans. Magnet.*, Vol. 44, No. 11, pp. 4057–4061, November 2008.

10. Lin, R., and Arkkio, A., "Calculation and analysis of stator end-winding leakage inductance of an induction machine," *IEEE Trans. Magnet.*, Vol. 45, No. 4, pp. 2009–2014, April 2009.

11. Tounzi, A., Henneron, T., Le Menach, Y., Askour, R., Dumetz, E., and Piriou, F., "3-D approaches to determine the end winding inductances of a permanent-magnet linear synchronous motor," *IEEE Trans. Magnet.*, Vol. 40, No. 2, pp. 758–761, March 2004.

12. Arshad, W. M., Lendenmann, H., Liu, Y., Lamell, J.-O. and Persson, H., "Finding end winding inductances of MVA machines," *Proceedings of 40th Annual Meeting of the IEEE Industry Applications Society*, pp. 2309–2314, Kowloon, Hong Kong, 2–6 October 2005.

13. Li, Y. B., Ho, S. L., Fu, W. N., and Liu, W. Y., "An interpolative finite-element modeling and the starting process simulation of a large solid pole synchronous machine," *IEEE Trans. Magnet.*, Vol. 45, No. 10, pp. 4605–4608, October 2009.

14. Freese, M., "Comparison between an analytic method and a numerical calculation to determine the end winding inductances of a turbo generator," *Proceedings of 19th International Conference on Electrical Machines (ICEM)*, Rome, Italy, 6–8 September 2010.

15. Dornau, U., *Berechnung und Messung der Stirnstreuung von Asynchronmaschinen mit Käfigläufer* [*Calculation and Measurement of End Winding Leakage of Induction Machines with Squirrel Cage*], Ph.D. Thesis, Dortmund University of Technology, Germany, 1990.

16. Ban, D., Žarko, D., and Mandić, I., "Turbogenerator end-winding leakage inductance calculation using a 3-D analytical approach based on the solution of Neumann integrals," *IEEE Trans. Energy Convers.*, Vol. 20, No. 1, pp. 98–105, March 2005.

17. Freese, M., "Analytic calculation of turbo generator end winding inductances using Neumann's formula," *Proceedings of 20th International Symposium on Power Electronics, Electrical Drives, Automation and Motion (SPEEDAM)*, Pisa, Italy, 14–16 June 2010.

18. Hsieh, M.-F., Hsu, Y.-C., Dorrell, D. G., and Hu, K.-H., "Investigation on end winding inductance in motor stator windings," *IEEE Trans. Magnet.*, Vol. 43, No. 6, pp. 2513–2515, June 2007.

19. Rosa, E. B., "The self and mutual inductances of linear conductors," *Bull. Nat. Bur. Standards*, Vol. 4, No. 2, pp. 301–344, 1908.

20. Carpenter, C. J., "The application of the method of images to machine end-winding fields," *Proc. IEE Part A: Power Eng.*, Vol. 107, No. 35, pp. 487–500, October 1960.

21. Williamson, S., and Mueller, M. A., "Calculation of the impedance of rotor cage end rings," *IEE Proc. B*, Vol. 140, No. 1, pp. 51–60, January 1993.

22. Hoffmann, S., *Untersuchung der Stromverdrängung in den Stäben, Stabüberständen und den Kurzschlussringen des Läufers einer Asynchronmaschine* [*Investigation of Current Displacement in Bars, Bar Overhang and End Rings of Induction Machines*], Ph.D. Thesis, Helmut Schmidt University of the Federal Armed Forces Hamburg, Germany, 2010.

23. Oeding, D., and Feser, K., "Mittlere geometrische Abstände von rechteckigen Leitern" [Mean geometric distances of rectangular conductors], *ETZ-A*, Vol. 86, No. 16, pp. 525–533, 1965.

24. Nürnberg, W., *Die Prüfung Elektrischer Maschinen* [*Inspection of Electrical Machines*], Berlin/Göttingen/Heidelberg: Springer, p. 156, 1955.

25. Aoulkadi, M., *Experimental Determination of Stray Load Losses in Cage Induction Machines*, Ph.D. Thesis, Darmstadt University of Technology, Germany, 2011.